against FSRM predictions using a constant value $R_{\text{eff}} = 0.96$ for all cases. Good agreement is observed between the DIII-D database and FSRM predictions, implying that the FSRM is sufficiently accurate to replicate the dynamics of the ELMy particle flux. Similar observations are observed for the ELM energy fluence [8].

The FSRM provides sufficient information about the ELM plasma conditions at the divertor target to make predictions of the time-dependent PFC sputtering rate. For W PFCs in DIII-D, this includes physical sputtering caused by free-streaming D and C ions originating from the pedestal top, and by D and C ions recycling from the divertor surface. The total W sputtering rate can be characterized as

$$\Gamma_W(t) = Y_{D\to W}\left(E_{D^+,FS}, t\right)\Gamma_{D^+,FS}(t) + Y_{D\to W}\left(E_{D^+,rec}, t\right)\Gamma_{D^+,rec}(t) + \sum_n Y_{C\to W}\left(E_{C^{n+},FS}, t\right)\Gamma_{C^{n+},FS}(t) + \sum_n Y_{C\to W}\left(E_{C^{n+},rec}, t\right)\Gamma_{C^{n+},rec}(t) \quad (1)$$

where the first and second terms account for sputtering due to the free-streaming and recycling D^+, and the third and fourth terms account for the C impurity flux for all charge states n. Physical sputtering yields Y are calculated with the SDTrim.SP code using a 45° ion impact angle. Impact energies for the free-streaming ions are directly predicted by the FSM, and for recycling ions, a Maxwellian energy spectrum plus sheath potential $3nT_{e,div}$ is used. The C impurity at the pedestal top is assumed fully stripped with a density equal to 2% of $n_{e,ped}$, in line with measurements from the DIII-D edge charge exchange recombination spectroscopy system [9, 18]. The recycled C ion impurity flux is assumed to be all C^{2+} ions, with is approximately the average charge state predicted by modeling [19, 20]. The stoichiometric fraction of C (due to implantation) in the top W surface layers is assumed equal to 0.5, in line with the results of previous studies [21, 22], which effectively reduces the predicted W sputtering rate by a factor of 2.

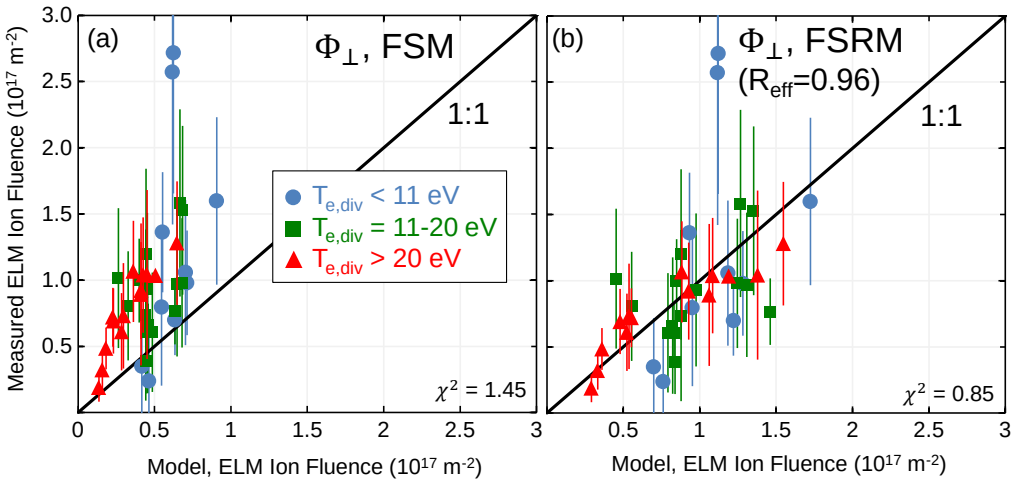

FIG 2. Experimental values of ELM ion fluence (measured by a Langmuir probe) plotted against (a) FSM calculations, (b) FSRM calculations with $R_{\text{eff}} = 0.96$.

3. EXPERIMENTAL MEASUREMENTS OF W SPUTTERING DURING ELMS IN DIII-D

As discussed above, tungsten gross erosion has been monitored spectroscopically during DIII-D DiMES experiments [8] and during the MRC [9, 23] with high spatial and temporal resolution. The predicted gross erosion rate of W during ELMs, based on Equation (1), is plotted in Figure 3a for typical DIII-D pedestal and divertor conditions. The W sputtering contribution from each term in Equation (1) is shown. The free-streaming D and C ions account for nearly all of the W erosion. Although these ions only represent a small fraction of the ion flux to the target, the high physical sputtering yield of these ions, due to their high impact energy, implies that they cause significant W sputtering. Recycling C2+ ions still receive sufficient energy from the $6T_e$ sheath potential to cause some erosion of W. The W erosion resulting from recycling D+ ions is zero because these ions have very low impact energies, below the threshold for D→W physical sputtering.

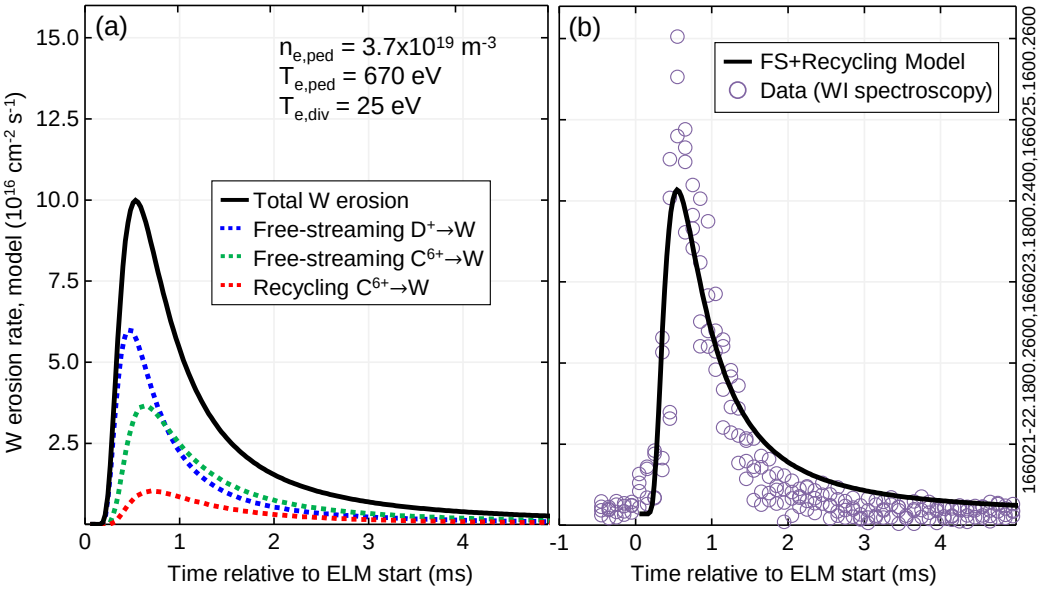

FIG 3. (a) Contributions to the W gross erosion rate through the ELM cycle from each sputtering mechanism, calculated by the FSRM. (b) Comparison of the FSRM calculation to experimental data.

The measured gross erosion rate of W for this condition, acquired during H-mode plasma bombardment of a W-coated DiMES sample, is shown in Figure 3b. The W erosion rate shows the characteristic sharp rising edge and exponential decay phase associated with ELM events. After the ELM ends, the W erosion rate dips slightly below its value before the ELM start. This may be due to a "cold-pulse" dynamic, as described in [24], where $T_{e,div}$ decreases just after the ELM event, leading to a decrease of the sheath potential and thus less W sputtering. The total W erosion rate predicted by the FSRM is overlaid on the experimental measurements in Figure 3b. Reasonable agreement is observed between calculated and measured W erosion rates, although the measurements do indicate a sharper peak that is not present in the FSRM predictions, Equation (1). This may be due to fast ions, which are not included in the FSRM, but which are expected to increase W sputtering early in the ELM phase [8]. The model may also somewhat over-predict the decay time of the W sputtering rate, which may also be due to the cold-pulse behavior described above.

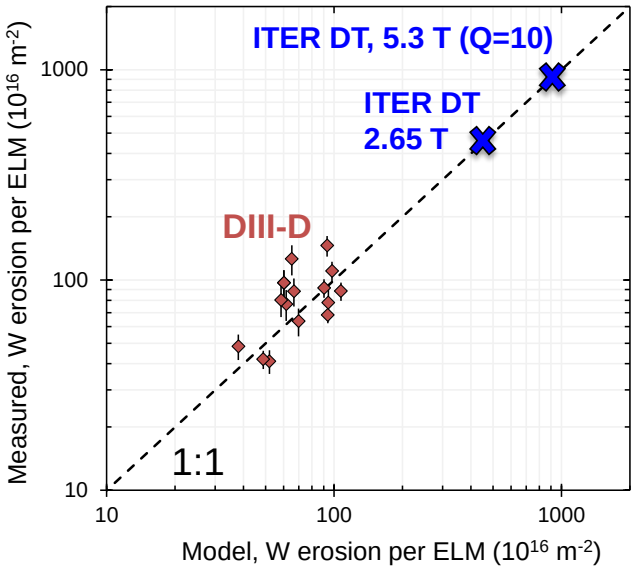

FIG 4. Measured values of total eroded W fluence per ELM event, plotted against the calculated values from the FSRM, Equation (1). Extrapolations to ITER parameters (Section 4) are also overlaid.

For the purposes of more thoroughly benchmarking of the FSRM predictions of W erosion, a dedicated experiment was performed during the MRC to develop a database of W gross erosion rates versus pedestal and ELM conditions. The Outer Strike Point (OSP) was placed on the inboard edge of the shelf ring. The diagnostic setup for this experiment is shown in Figure 1b. The pedestal conditions and ELM frequency were modified by

changing the input power and upper triangularity, while keeping the divertor conditions relatively constant. Pedestal conditions ranged between $T_{e,ped}$ = 320-650 eV and $n_{e,ped}$ = 3.7-7.4x10^{19} m^{-3}, and ELM frequencies ranged from approximately 10-100 Hz. In Figure 4, the calculated, time-integrated W erosion fluence per ELM is plotted against the calculations from the FSRM. Good agreement is observed between the FSRM predictions and the experimental measurements over the range of pedestal conditions and ELM frequencies explored. The level of agreement observed between the FSRM and experimental measurements provides a level of validation for the model developed in Section 2 and lends credibility to the extrapolation of the FSRM W erosion model to ITER, described in the next section.

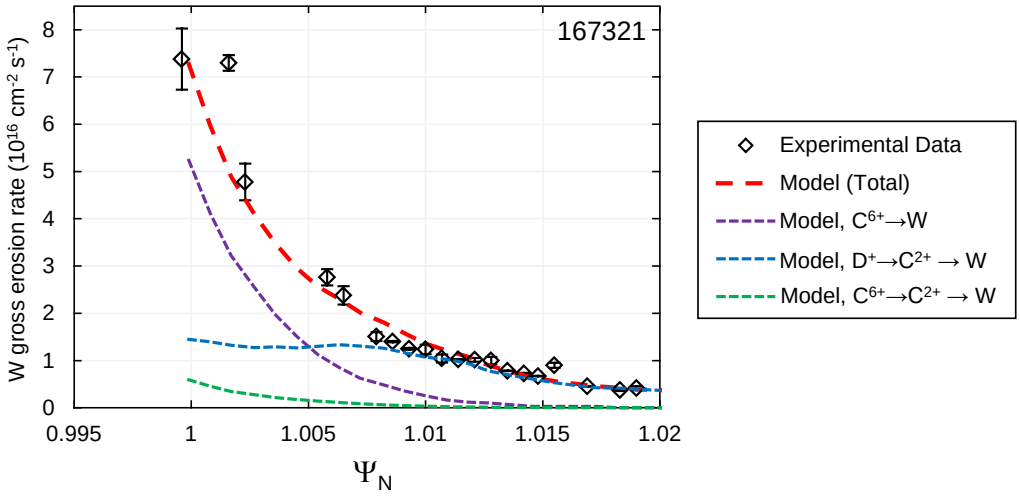

FIG 5. Spatial profile of the intra-ELM W gross erosion rate for shot 167321, both calculated with the semi-analytic model in [9] *and fit to the experimental data. Calculated contributions to the overall W erosion rate from different sputtering mechanisms are also overlaid.*

Experimental studies of the *spatial* dependence of the gross erosion rate of W during ELMs have also recently been performed using a semi-analytic model similar to the FSRM [9]. Since the FSM only attempts to describe parallel ELM dynamics, empirical fitting parameters are introduced to describe the radial decay of the intra-ELM C impurity flux. The radial profile of the average D and C ion impact energies during ELMs are inferred from experimental measurements, neglecting the contribution of recycling ions to the impact energy profile. In Figure 5, the calculated tungsten gross erosion rate is plotted as a function of normalized flux coordinates Ψ_N, averaged over the full ELM cycle. The spatial profile of the modeled intra-ELM W erosion rate is compared to the experimentally measured W erosion rate, inferred via WI imaging [23]. A characteristic exponential decay length of the C^{6+} impurity flux equal to half that of the measured D^+ ion flux is needed to achieve consistency between the experimental data and the model calculations. Investigations into differences between the cross-field impurity and main ion transport during ELMs are ongoing.

In Figure 5 the contributions to the W erosion rate due to free-streaming C^{6+} ions, as well as recycling C^{2+} (eroded by both D and C) are also identified. It is inferred that close to the OSP, the gross erosion rate of W is largely dominated by the free-streaming C^{6+} ions, but in the far-target region (Ψ_N > 1.01, ~ λ_q away from OSP) the contribution of the recycling C^{2+} to the overall gross W erosion rate can be significant. This "ELM-average" model concludes that physical sputtering of W directly by D during ELMs is minimal, in contrast with some other studies on JET-ILW [4, 6] and DIII-D [8]. However, it is noted that effect of D is indirectly incorporated, as D ion impacts cause additional C erosion and re-deposited C ions further enhance W gross erosion. Importantly, model validation studies of both the time and spatial dependence of intra-ELM gross W erosion results suggest that understanding the free-streaming ion transport from the pedestal to the divertor is essential to capture the physics of intra-ELM W sourcing.

4. DISCUSSION AND IMPLICATIONS FOR ITER

In Section 2 of this paper, it is demonstrated that fast particle recycling is largely responsible for the strong increase in divertor electron density and ion flux that occurs during ELMs in DIII-D. Recent JET-ILW results [16] indicate particle recycling does not strongly affect the divertor ion flux during ELMs, because the mean energy of recycled neutrals during ELMs is large on the smooth bulk W surfaces comprising the JET-ILW divertor. This implies that charge exchange is the dominant neutral-to-ion conversion mechanism in JET-ILW,

producing minimal additional ion current during ELMs. In DIII-D, however, the rough graphite or W-coated graphite divertor surfaces produce neutrals with substantially lower mean impact energy, and thus the primary volumetric sink of neutral D atoms in DIII-D will be electron impact ionization [8].

In Section 3, good agreement was obtained between experimental measurements of the total number of sputtered W atoms during ELMs and the predictions of the FSRM across a range of DIII-D pedestal conditions. It was inferred for one particular case (Figure 3) that the gross erosion of W was dominated by the free-streaming D^+ and C^{6+} ions, with relatively little contribution from the recycling ion species. As an extension of this result, it is useful to understand how the FSRM predicts the contribution to the overall W erosion rate will change as a function of pedestal and divertor conditions. In Figure 6, the fractional contributions of free-streaming D^+ ions, free-streaming C^{6+} ions, and recycling C^{2+} ions are plotted against the typical range of pedestal temperatures achieved on DIII-D. Both a case of relatively low divertor temperature ($T_{e,div}$ = 10 eV) and high divertor temperature ($T_{e,div}$ = 30 eV) are included for comparison. Note that recycling D^+ ions do not have sufficient impact energy to sputter W atoms in these cases and their contribution remains zero for all values of $T_{e,ped}$ and both values of $T_{e,div}$ displayed.

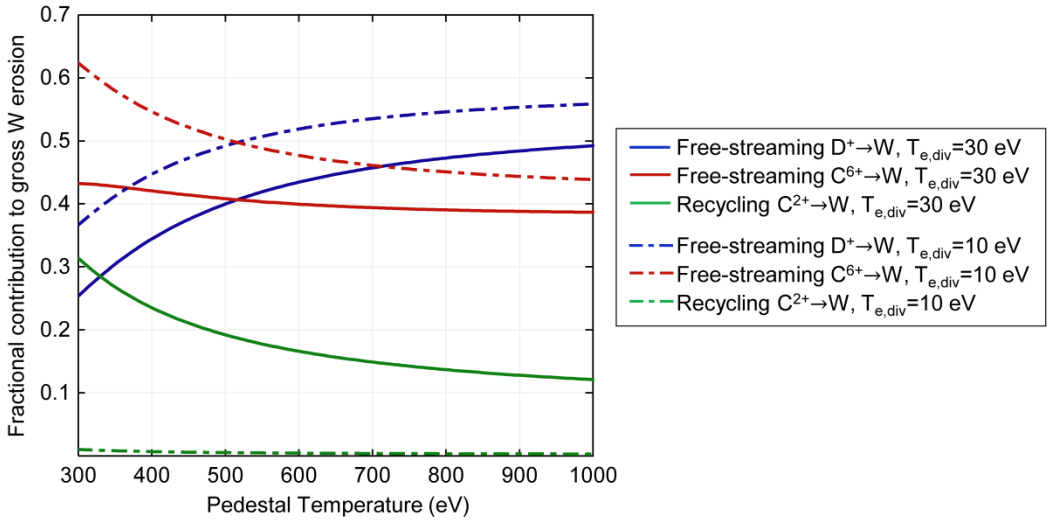

FIG 6. Fractional contributions of each W erosion mechanism to the gross erosion rate of tungsten during ELMs, calculated with the FSRM, as a function of typical DIII-D divertor and pedestal temperatures.

For the high $T_{e,div}$ case, all three W erosion pathways contribute roughly equally to the W sputtering rate at low pedestal temperature ($T_{e,ped}$= 300 eV). As $T_{e,ped}$ increases, the fractional contribution of the free-streaming D^+ ions to the overall gross W erosion rate increases, while the contribution of free-streaming C^{6+} and recycling C^{2+} ions decreases. This transition occurs because the physical sputtering yield of D on W increases strongly with ion impact energy (proportional to $T_{e,ped}$) in this regime, while the sputtering yield of C on W is relatively constant [8]. For the low $T_{e,div}$ case, the contribution of recycling C^{2+} ions to the W erosion rate is negligible for all pedestal temperatures. This is because a divertor electron temperature of 10 eV results in recycling C^{2+} ions with impact energies very close to the threshold for C→W physical sputtering. The fractional contributions of the free-streaming species show similar trends to the high $T_{e,div}$ case, with free-streaming C^{6+} being the most important contributor at low values of $T_{e,ped}$, but free-streaming D^+ becoming progressively more important as pedestal temperature increases. Note that in the FSRM formulation, all W erosion rates during ELMs are linearly proportional to pedestal density, and thus $n_{e,ped}$ does not affect the fractional contributions to the overall W erosion rates displayed in Figure 6.

Finally, because the FSRM calculations for W sputtering during ELMs are fully predictive, it is useful to extrapolate what gross W erosion rates may be expected during unmitigated ELMs in ITER. In developing these extrapolations, the same assumptions regarding L_{ELM}, $L_{\parallel}$, and R_{eff} used in the DIII-D cases are applied to the ITER geometry. The standard ITER reference magnetic equilibrium is utilized (with salient features described in [25, 26]) and the electron temperature at the outer divertor target is set to 5 eV. A full-field (B_T = 5.3 T) and half-field (B_T = 2.65 T) case are studied, with pedestal density and temperature taken from Table 2 in [14]. For the half-field case, all magnetic field components simply scaled down by a factor of 0.5 to keep the pitch angles of all magnetic field lines constant between both cases. No toroidal shaping of the divertor tiles is incorporated, as the emphasis is on general trends, but arbitrary shaping effects could be incorporated in a straightforward

manner. A 0.5% Be^{4+} concentration at the pedestal top and a 0.5% Be^{2+} flux fraction at the outer divertor target are assumed, similar to the values inferred on JET-ILW [27]. The main ions in these calculations are D and T in a 1:1 ratio. No other pedestal or divertor impurities are considered; e.g., the effect of W→W self-sputtering is neglected. W self-sputtering by prompt W re-deposition has been shown to be small in ERO simulations of ELMs in the JET-ILW divertor [28], but the effect of free-streaming W ions from the pedestal top during ELMs in JET-ILW and ITER may warrant further study due to the efficiency of self-sputtering.

The calculated time evolution of the W erosion rate during unmitigated ELMs at the ITER outer divertor target is shown for these two cases in Figure 7, with the contributions from D, T, and Be overlaid. The peak W sputtering rate caused by each species occurs at a slightly different time because the free-streaming ion velocity is inversely proportional to atomic mass, but the time delay between the three peaks is small (~0.1 ms) relative to the total ELM time. More importantly, the FSRM predicts gross W erosion during ELMs in ITER will be dominated by free-streaming D^+ and T^+ ions, with only a small contribution from free-streaming Be^{4+} ions and zero contribution from recycling ions. This implies that extrapolations of the W divertor impurity source during ELMs in ITER are insensitive to the Be impurity fraction in the plasma. The contribution from free-streaming T^+ is approximately 2x larger than free-streaming D^+ due to the higher physical sputtering yield of T on W.

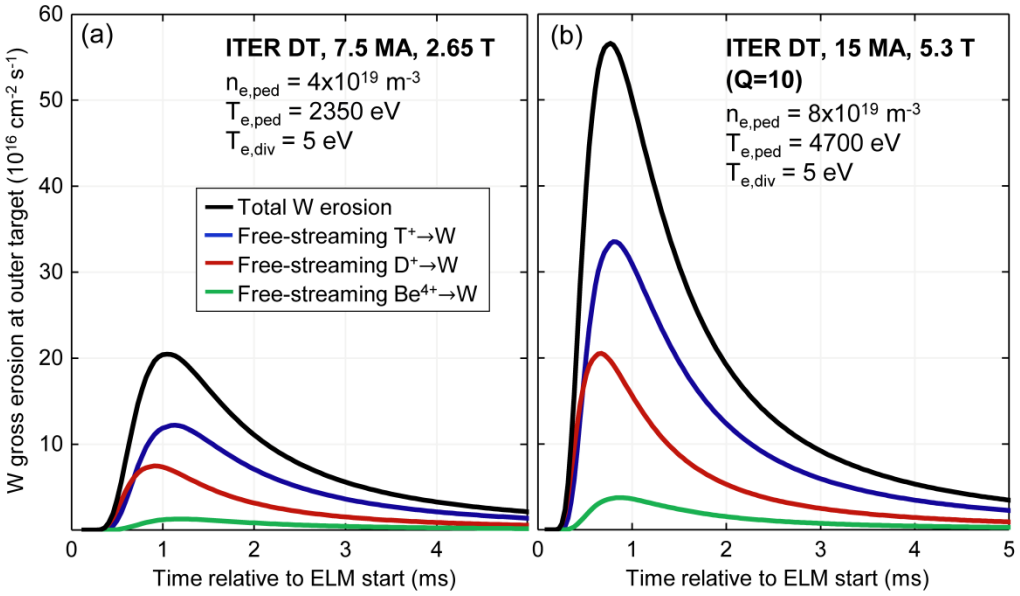

FIG 7. Predicted time evolution of the gross W erosion rate at the ITER outer divertor target for (a) the ITER half-field case, (b) the ITER full-field (DT Q=10) case. The contributions to the total W sputtering rate from each of the three free-streaming ion species is also provided.

As expected, the peak and integrated W erosion during the full-field cases is substantially larger than the half-field case. However, despite a 4x increase in pedestal pressure, only about a 2x increase in total W erosion occurs because these high values of $T_{e,ped}$ correspond to the "plateau" regime of W sputtering yields, where increasing ion impact energy does not materially affect the sputtering yield of W by D, T, or Be. The total W erosion per ELM for each ITER case is plotted with the DIII-D results in Figure 4. The FSRM predicts that approximately 10x more W atoms will be sputtered per m^2 in the ITER divertor compared to DIII-D. While this may seem alarming in the context of the strict core W contamination limits for ITER, core plasma volume scales as R^3 while the divertor plasma-wetted area only scales with R. Thus the ratio of core volume to divertor plasma-wetted area will be larger in ITER by a factor of about $(R_{\mathrm{ITER}}/R_{\mathrm{DIII-D}})^2$ ~ 13, which roughly cancels out the order of magnitude increase in W erosion fluence expected for ITER. Additionally, ITER will be operated with either mitigated or small ELMs, which may greatly reduce W sourcing.

Finally, it is noted that this paper presents solely calculations of the gross W erosion rate during ELMs. Understanding the net W erosion rate during ELMs involves a complex, time-dependent interplay of the sputtered atom ionization lengths, the gyro-motion of each W charge state in the near target region, and the effect of the magnetic pre-sheath. As discussed above, ERO simulations indicate that the W prompt re-deposition fraction during ELMs is likely even larger than the inter-ELM phase because the high target electron densities during ELMs result in very short ionization mean free paths [28]. These studies, however, were performed with static, "ELM-average" plasma conditions and further work must be performed to model W net erosion during ELMs using a realistic model for how the background divertor plasma evolves with time.

5. SUMMARY

The Fundamenksi-Moulton 'free-streaming' model for ELM dynamics was described and refined to account for the impact of particle recycling during ELMs, the FSRM. It was shown that incorporating recycling is needed to account for the total ion fluence measured during ELMs in the DIII-D divertor. The FSRM was extended to make predictions for W sputtering in the divertor during ELMs, which includes the free-streaming and recycling main ions and impurities. The FSRM predicts that the energetic free-streaming ions from the pedestal top dominate the total W sputtering rate during ELMs in DIII-D, except for very low temperature pedestals and high-temperature divertor targets. Direct validation of the FSRM calculations of the W gross erosion rate during ELMs were performed in DIII-D using WI spectroscopy measurements and agreement was observed between the FSRM and experimental data. The FSRM calculations were extrapolated to ITER DT scenarios, and it was determined that W sputtering at the outer divertor targets during unmitigated ELMs in ITER will likely be dominated by free-streaming D^+ and T^+ ions, with little contribution from the Be impurity. Future studies will focus on extending the FSRM to mitigated ELM regimes and to a deeper understanding of the additional physics regulating high-Z impurity transport throughout the unconfined plasma volume.

ACKNOWLEDGEMENTS

The author would like to thank Dr. Christophe Guillemaut, Dr. Jerome Guterl and Dr. Igor Bykov for valuable discussions and contributions.

This material is based upon work supported by the U.S. Department of Energy, Office of Science, Office of Fusion Energy Sciences, using the DIII-D National Fusion Facility, a DOE Office of Science user facility, under Awards DE-FC02-04ER54698, DE-AC52-07NA27344, DE-AC05-00OR22725, and DE-FG02-07ER54917. DIII-D data shown in this paper can be obtained in digital format by following the links at https://fusion.gat.com/global/D3D_DMP.

REFERENCES

[1] R.A. Pitts et al., Phys. Scr. T138 (2009) 014001.

[2] T. Putterich et al., Nucl. Fusion 50 (2010) 025012.

[3] R.P. Dux et al., J. Nucl. Mater. 390–391 (2009) 858–863.

[4] N. Den Harder et al., Nucl. Fusion 56 (2016) 026014.

[5] S. Brezinsek and JET-EFDA contributors, J. Nucl. Mater. 463 (2015) 11–21 .

[6] C. Guillemaut et al., Phys. Scr. T167 (2016) 014005.

[7] I. Borodkina et al., Phys. Scr. T170 (2017) 014065.

[8] T. Abrams et al., "Experimental validation of a model for particle recycling and tungsten erosion during ELMs in the DIII-D divertor" Nucl. Mater. Energy (2018) submitted.

[9] G. Xu et al., "Study of DIII-D tungsten erosion processes by using a carbon-tungsten mixed material model," Nucl. Mater. Energy (2018) submitted.

[10] W. Fundamenski et al., Plasma Phys. Control. Fusion 48 (2006) 109–156.

[11] D. Moulton et al., Plasma Phys. Control. Fusion 55 (2013) 085003.

[12] C.P.C. Wong et al., J. Nucl. Mater. 196–198 (1992) 871.

[13] K. Holtrop et al., Fusion Sci. Tech. 72 (2017) 634-639.

[14] T. Eich et al., Nucl. Mater. Energy 12 (2017) 84–90.

[15] G.T.A. Huysmans et al., Plasma Phys. Control. Fusion 51 (2009) 124012.

[16] C. Guillemaut et al., Nucl. Fusion 58 (2018) 066006.

[17] I. Bykov et al., "ELM-resolved characterization of the fuel and impurity source in the divertor of DIII-D" Nucl. Fusion (2018) to be submitted.

[18] C. Chrystal et al., Rev. Sci. Instrum. 87 11E512 (2016).

[19] J.N. Brooks et al., Fusion Eng. Des. 94 (2015) 67–71.

[20] T. Abrams et al., Nucl. Fusion 57 (2017) 056034.

[21] R. Ding et al., Nucl. Fusion 57 (2017) 056016.

[22] J. Guterl et al., Nucl. Mater. Energy 12 (2017) 392–398.

[23] T. Abrams et al., IEEE T. Plasma Sci. 46 (2018) 1298-1305.

[24] C. Guillemaut et al., Plasma Phys. Control. Fusion 57 (2015) 085006.

[25] T. Eich et al., Nucl. Fusion 53 (2013) 093031.

[26] J.P. Gunn et al., Nucl. Fusion 57 (2017) 046025.

[27] G.J. van Rooij et al., J. Nucl. Mater. 438 (2013) S42–S47.

[28] A. Kirschner et al., Plasma Phys. Control. Fusion 60 (2018) 014041.